Low-Power and Field-Free Perpendicular Magnetic Memory Driven by Topological Insulators

Baoshan Cui, Aitian Chen,* Xu Zhang, Bin Fang, Zhaozhuo Zeng, Peng Zhang, Jing Zhang, Wenqing He, Guoqiang Yu, Peng Yan, Xiufeng Han, Kang L. Wang, Xixiang Zhang,* and Hao Wu*

Giant spin–orbit torque (SOT) from topological insulators (TIs) has great potential for low-power SOT-driven magnetic random-access memory (SOT-MRAM). In this work, a functional 3-terminal SOT-MRAM device is demonstrated by integrating the TI [(BiSb)$_2$Te$_3$] with perpendicular magnetic tunnel junctions (pMTJs), where the tunneling magnetoresistance is employed for the effective reading method. An ultralow switching current density of 1.5×10^5 A cm^{-2} is achieved in the TI-pMTJ device at room temperature, which is 1–2 orders of magnitude lower than that in conventional heavy–metals-based systems, due to the high SOT efficiency $\theta_{SH} = 1.16$ of (BiSb)$_2$Te$_3$. Furthermore, all-electrical field-free writing is realized by the synergistic effect of a small spin-transfer torque current during the SOT. The thermal stability factor ($\Delta = 66$) shows the high retention time (>10 years) of the TI-pMTJ device. This work sheds light to the future low-power, high-density, and high-endurance/retention magnetic memory technology based on quantum materials.

1. Introduction

In the past century, magnetic memory played a crucial role in information technology, such as magnetic hard disk drive (HDD) that serves as the major data storage technology until now. Besides HDD, magnetic random-access memory (MRAM) is considered as a promising candidate for the next-generation memory technology beyond complementary metal–oxide–semiconductor (CMOS), due to the nonvolatility, low-power ($\approx$fJ), high-speed ($\approx$ns), and the potential for logic-in-memory computing.[1] For MRAM, the magnetic tunnel junctions (MTJs) are basic storage unit, and the information is stored based on the relative magnetization orientations of the recording and reference layers (parallel for bit "0"and antiparallel for bit "1"), where the tunneling magnetoresistance (TMR) provides an effective reading method electrically.[2–6] However, current spin-transfer-torque (STT) MRAM (STT-MRAM) suffers from the reliability and endurance issues induced by the high writing current density across the thin MgO barrier,[7,8] therefore, the 3-terminal spin–orbit torque (SOT) MRAM (SOT-MRAM) with separated writing and reading paths will significantly improve the endurance of MRAM.[9–15]

In a typical SOT structure, the charge-current flowing in the non-magnetic layer with strong spin–orbit coupling (SOC) will be converted to a transverse spin current which is injected to the adjacent ferromagnetic layer and exerts a torque to drive the magnetization switching. Recently, the orbital torque generated by the orbital current injection from the weak-SOC metal has also been demonstrated in nonmagnet/ferromagnet systems (Note S1, Supporting Information).[16–18] The charge–spin conversion efficiency (θ_{SH}) dominates the power consumption of a SOT device, however, in classical materials, the spin Hall/Rashba induced θ_{SH} is limited (<1) due to the spin-dependent scattering mechanism.[19–27] In quantum materials, such as topological insulators (TIs) with the insulating bulk and conducting surface

B. Cui, X. Zhang, J. Zhang, W. He, G. Yu, X. Han, H. Wu
Songshan Lake Materials Laboratory
Dongguan, Guangdong 523808, China
E-mail: wuhao1@sslab.org.cn

P. Zhang, K. L. Wang, H. Wu
Department of Electrical and Computer Engineering
University of California, Los Angeles
Los Angeles, CA 90095, USA

A. Chen, B. Fang, X. Zhang
Physical Science and Engineering Division
King Abdullah University of Science and Technology
Thuwal 23955–6900, Saudi Arabia
E-mail: aitian.chen@kaust.edu.sa; xixiang.zhang@kaust.edu.sa

B. Cui, W. He, G. Yu, X. Han, H. Wu
Beijing National Laboratory for Condensed Matter Physics
Institute of Physics
Chinese Academy of Sciences
Beijing 100190, China

Z. Zeng, P. Yan
School of Electronic Science and Engineering and State Key Laboratory of Thin Films and Integrated Devices
University of Electronic Science and Technology of China
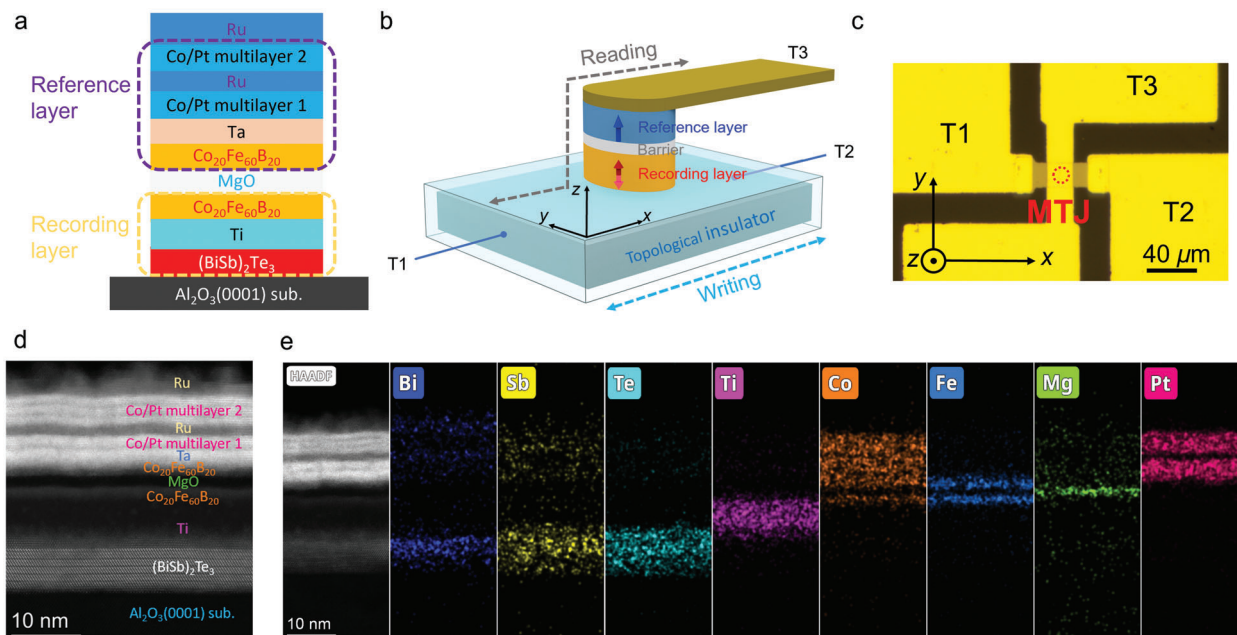Chengdu 610054, China

Figure 1. Schematic of the TI-based perpendicular SOT-MRAM cell. a) Schematic of the structure of the TI-pMTJ stack. b) Schematic of the 3-terminal SOT-MRAM cell based on a TI. The writing current is applied between the T1–T2 channel to switch the recording layer by SOT, while the tunneling magnetoresistance (TMR) is employed as the reading method by applying a small dc current of 50 µA between the T1–T3 channel. c) Microscopy picture of the patterned SOT-MRAM device, where MTJ is marked by the red-dotted circle with the diameter of 3 µm and the bottom TI layer with a width of 20 µm servers as the SOT channel. d) Cross-sectional TEM image of the TI-pMTJ stack shows the layer-by-layer structure of TI, the clear interface between TI and MTJ, and the clear interface between CoFeB and MgO barrier. e) High-angle annular dark-field (HAADF) image and energy-dispersive X-ray (EDX) mappings of the TI-pMTJ stack.

states, the interconversion between orbital and spin momentum (spin-momentum locking) in the topological surface states produces a giant θ_{SH}, promising for the future ultralow-power SOT devices.[28–35]

A great interest has been focused on the TI/FM heterostructures in the Hall-device level for improving the basic SOT performances.[32,36–39] For practical SOT-MRAM with efficient reading signals, the integration of TIs with MTJs is in great demand for the TI-driven SOT-MRAM technology, where the SOT performance in the TI-MTJ-device level is very important for the future industrial applications. However, due to the challenges of the integration of TI and MTJ stacks, such as the chemical degradation of TI quality during the device fabrication and the interfacial diffusion during the annealing, the correlative reports so far are only limited to the preliminary TI-iMTJ devices with the in-plane magnetic anisotropy.[33] TI-pMTJ devices with perpendicular magnetic anisotropy (PMA) have much higher thermal stability and much lower switching current density, and thus are more desirable for scaling-down devices to realize low-power and high-density SOT-MRAM applications.

In this article, we experimentally demonstrate the functional 3-terminal SOT-MRAM device based on TI-pMTJ, with an ultralow critical switching current density of 1.5×10^5 A cm^{-2} at room temperature, which is 1–2 orders of magnitude lower than that in the heavy metal-based SOT-MRAM device. A θ_{SH} of 1.16 in TI is quantified by the harmonic Hall measurements, supporting the ultralow switching current density. With applying a small STT current during the SOT operation to break the inversion symmetry, the all-electrical field-free switching is realized by

the synergistic effect of STT + SOT, at the same time the critical switching current density of SOT is further reduced to the order of 10^4 A cm^{-2}, which is re-produced by the micromagnetic simulations. This work demonstrates the TI-driven SOT-MRAM with ultralow writing current density and high thermal stability, inspiring the revolution of SOT-MRAM from classical to quantum materials.

2. Results and Discussion

The film stacks consist of: i) $(BiSb)_2Te_3(6)/Ti(5)/Co_{20}Fe_{60}B_{20}(1)/$ MgO(1.6)/$Co_{20}Fe_{60}B_{20}(1.1)/Ta(0.5)/[Co(0.4)/Pt(1.5)]_2/Co(0.4)/$ Ru(0.85)/$[Co(0.4)/Pt(1)]_3/Ru(5)$ and ii) $(BiSb)_2Te_3(6)/Ti(5)/Co_{20}$-$Fe_{60}B_{20}(1)/MgO(2)/Ta(2)$ (thickness in nanometers), in which the TIs of $(BiSb)_2Te_3$ were epitaxially grown by MBE on the $Al_2O_3(0001)$ substrate and the MTJ stacks were prepared by the magnetron sputtering under the base pressure lower than 1×10^{-6} Pa. The spin diffusion length (λ_s) of Ti is ≈13.3 nm, thus, the spin current generated by the topological surface states in $(BiSb)_2Te_3$ can pass through the 5 nm Ti layer efficiently with the transmission ratio around $e^{-5/13.3} = 69\%$.[40–43] Then, the films (i) were patterned into the 3-terminal SOT-MRAM devices (i.e., TI-pMTJ devices) by electron-beam and photolithography combined with Ar ion milling. Finally, the TI-pMTJ devices were annealed at 250 °C for 0.5 h in vacuum to enhance the PMA. All the measurements were carried out at room temperature.

Figure 1a shows the schematics of TI-pMTJ structure, in which the bottom perpendicularly magnetized $(BiSb)_2Te_3/Ti/Co_{20}Fe_{60}B_{20}/MgO$ stack servers as the record-
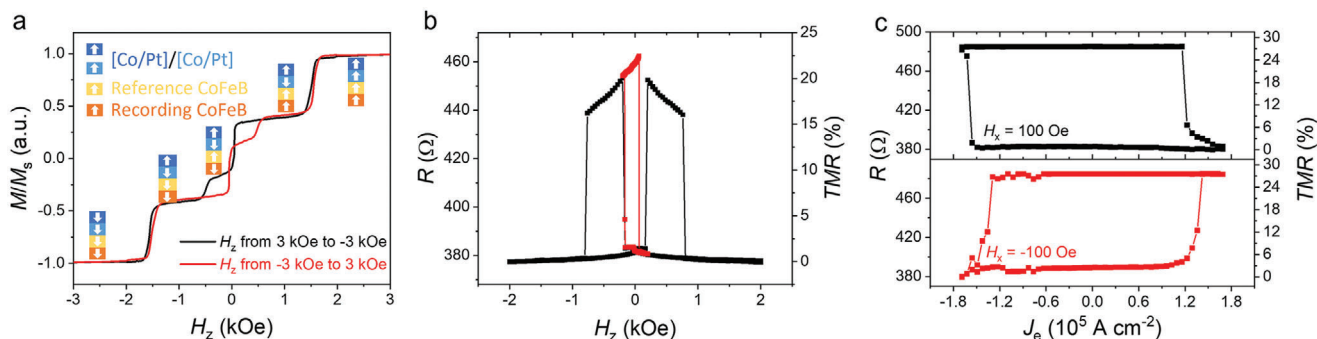
Figure 2. Magnetic properties and current-driven SOT switching in micro-sized TI-pMTJ devices. a) MH_z curves in TI-pMTJ stack, where the blue, yellow, and orange arrows represent the magnetization of the $[Co/Pt]_n$ multilayer, the top reference and bottom recording CoFeB layers, respectively. b) Tunneling resistance R and TMR ratio as a function of H_z (black curve) in TI-pMTJ device. The red minor R(TMR)–H loop represents the resistance switching from the CoFeB recording layer. c) Current-driven SOT switching in the TI-pMTJ device under the assisted magnetic field along the x axis (H_x) of ± 100 Oe, respectively.

ing layer. Figure 1b shows the 3-terminal SOT-MRAM cell with TI-pMTJ, in which the writing current is applied between terminal 1 (T1) and terminal 2 (T2) in TI layer to generate the spin current (J_s) from the topological surface states. Then, J_s passes through the light metal Ti layer and injects to the adjacent CoFeB layer, exerting SOTs and switching the magnetization with a sufficient current density. For reading, a small direct (dc) current of 50 µA is applied between the T1 and T3 channel (i.e., pass though the MTJ) to read the magnetization by the TMR. Figure 1c shows a microscopy image of the patterned SOT-MRAM device, where TI-pMTJ is located at the intersection region between the bottom (i.e., TI) and top electrodes (Ti/Au) and marked by the red-dotted circle with a diameter of 3 µm. Figure 1d presents the cross-sectional transmission electron microscopy (TEM) image of the TI-pMTJ stack, we can see the high-quality layer-by-layer structure of TI, the clear interface between TI and MTJ, and the clear interface between CoFeB and MgO barrier. Generally, the crystallinity of TIs is important for the quantum transport in topological surface states.[33,44,45] Besides, the high-angle annular dark-field (HAADF) image and energy-dispersive X-ray (EDX) mappings of MTJ sample (i) (see Figure 1e) also reveal that the interfaces of $(BiSb)_2Te_3$/Ti, Ti/CoFeB, and CoFeB/MgO/CoFeB are clear and sharp, supporting the high interfacial spin transparency.

The magnetic hysteresis (M–H) loop of sample i) measured by a superconducting quantum interfere device (SQUID) with the magnetic field applied along out-of-plane direction (H_z) is shown in **Figure 2**a, where the blue and orange arrows represent the magnetization states of two coupled $[Co/Pt]_n$ multilayers in the synthetic antiferromagnetic (SAF) structure and two CoFeB (recording and reference) layers, respectively. Four-step M–H curves clearly show the switching process of each layer individually, where the different coercivities of CoFeB recording layer and CoFeB reference layer support the parallel and antiparallel magnetization states, corresponding to a low resistance state ("0" state) and high resistance state ("1" state), respectively. Figure 2b shows the tunneling resistance R and the TMR ratio as a function of H_z in the TI-pMTJ device, and the red minor loop represents the resistance switching from the CoFeB recording layer, where a TMR ratio of 22% indicates the high-quality of the pMTJ on top of the TI surface.

Then, the current-driven SOT switching is performed in the same TI-pMTJ device shown in Figure 2b: the 1 ms writing current pulses are applied between the T1 and T2 channel to provide the SOT to switch the bottom recording CoFeB layer, with the assistance of an in-plane magnetic field $H_x = \pm 100$ Oe for the deterministic switching. After each writing pulse (1 s later), the tunneling resistance R of MTJ is measured to detect the magnetization state of the recording CoFeB layer by a small dc reading current of 50 µA between the T1 and T3 channel. Figure 2c shows the R and TMR ratio as a function of writing current density (J_e) in the TI layer. We can clearly see a nonvolatile high/low resistance switching in the TI-pMTJ device with a ΔTMR of 27%, where the opposite switching polarities at $H_x = \pm 100$ Oe indicate the standard SOT switching characteristic. We calculate the current density in TI by the parallel circuit model by considering the resistivity ρ of $(BiSb)_2Te_3$ (4.68×10^{-3} Ω cm), Ti (4.2×10^{-5} Ω cm), and $Co_{20}Fe_{60}B_{20}$ (1.65×10^{-4} Ω cm) (Note S2, Supporting Information). The obtained critical switching current density J_{cri} in $(BiSb)_2Te_3$ is 1.5×10^5 A cm^{-2}, which is 1–2 orders of magnitude lower than the typical values of 10^6 to 10^7 A cm^{-2} in heavy metal (HM)-based systems,[22,25–27] indicating the high charge–spin conversion efficiency in topological surface states.

The required in-plane external magnetic field to assist the SOT switching limits the practical application of SOT-MRAM in high-density integrated circuits. To achieve field-free SOT switching, we apply an additional small STT current between the T2 and T3 channel to break the inversion symmetry by the STT-induced out-of-plane spin polarization during the SOT, as shown in **Figure 3**a. Figure 3b demonstrates the field-free SOT switching with a STT current density J_{STT} of 1.2×10^4 A cm^{-2} in a nanoscale TI-pMTJ devices with a diameter of 800 nm, and the switched TMR ratio is up to ≈22%. Figure 3c shows the critical current density of field-free SOT switching ($J_{cri-SOT}$) as a function of J_{STT}, in which we found that $J_{cri-SOT}$ can be reduced by increasing the J_{STT}. It is worth noting that a small J_{STT} (as low as 2×10^3 A cm^{-2}) can still break the inversion symmetry for achieving the field-free SOT switching, which is important to reduce the MgO degradation and thus to improve the MTJ endurance. Besides, the influence of the STT current on the SOT current is negligible (Note S4, Supporting Information).
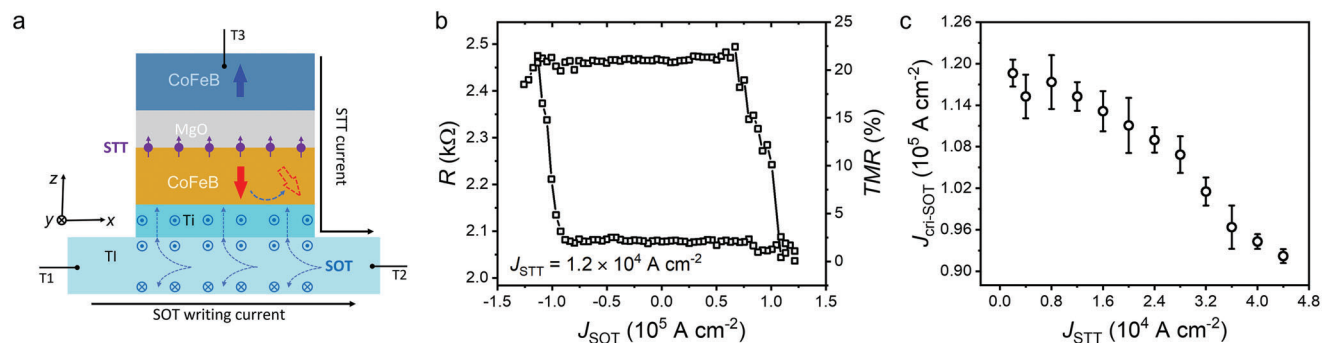
ADVANCED
SCIENCE NEWS
www.advancedsciencenews.com

ADVANCED
MATERIALS
www.advmat.de

Figure 3. Field-free writing by the interaction of spin-transfer torque (STT) and spin–orbit torque (SOT) currents. a) Schematic of 3-terminal STT + SOT driven TI-pMTJ device. b) Field-free SOT switching loop in the TI-pMTJ device under the assisted STT current density $J_{STT} = 1.2 \times 10^4$ A cm^{-2}. c) The critical current density of field-free SOT switching ($J_{cri-SOT}$) as a function of J_{STT}.

For a thorough understanding of such field-free switching mechanism in the 3-terminal TI-pMTJ device, we have performed micromagnetic simulations base on Landau-Lifshitz-Gilbert (LLG) equation with additional SOT and STT terms (the details see Note S5, Supporting Information). To simulate the real circumstance, the random material grains with the size of 10 nm are introduced in the micromagnetic simulations. **Figure 4**a represents the switching processes of perpendicular magnetization m_z in the disk with a diameter of 800 nm, where the applied $J_{STT} = 3.6 \times 10^5$ A cm^{-2} and $J_{SOT} = 6.7 \times 10^6$ A cm^{-2}. In this configuration, the field-free switching can be realized, though the SOT current shuts down at 20 ns. Moreover, the cases either only J_{STT} or only J_{SOT} are investigated (see Figure S3, Supporting Information), it is found that the STT current without a SOT current cannot switch the magnetization. Similarly,

though the large SOT current density can flip the magnetization into the in-plane, the magnetization cannot be deterministically switched without the STT current when the SOT current density shuts down. Hence, the STT current, even though very small, is the key point to realize the field-free SOT switching in the 3-terminal TI-pMTJ device. Moreover, the simulations illustrate that the switching process contain two steps: domain nucleation and domain wall propagation, as shown in Figure 4b. Then, the interplay of STT and SOT is studied and the results in Figure 4c show that the $J_{cri-SOT}$ decreases with the increases of J_{STT}, which is consistent with our experimental results in Figure 3c. Due to the nucleation and motion of the domain wall under the thermal fluctuation and material grain, the analytical results are mostly twice as large as the simulated results.
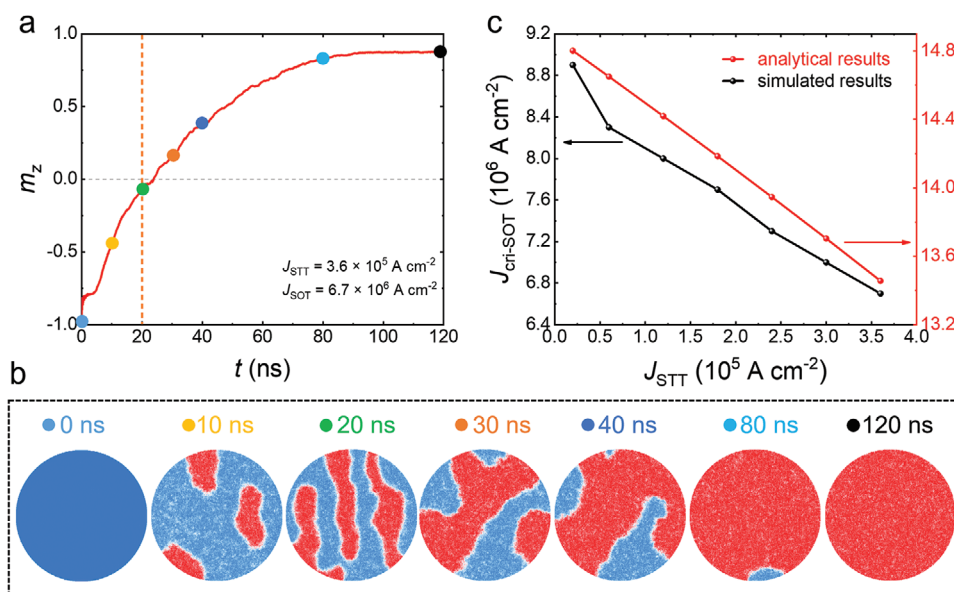

Figure 4. Micromagnetic simulation of field-free writing process by the combined STT and SOT currents. a) The reduced magnetization m_z as a function of time t with $J_{STT} = 3.6 \times 10^5$ A cm^{-2} and $J_{SOT} = 6.7 \times 10^6$ A cm^{-2}. The orange dotted line indicates the SOT current shutdown time. b) The magnetization distribution at different time. The teal and red represent the magnetic moment point down and up, respectively. c) The critical SOT switching current density $J_{cri-SOT}$ as a function of the STT current density J_{STT}. The red solid dots represent the analytical results, and the black solid dots indicate the simulated results.
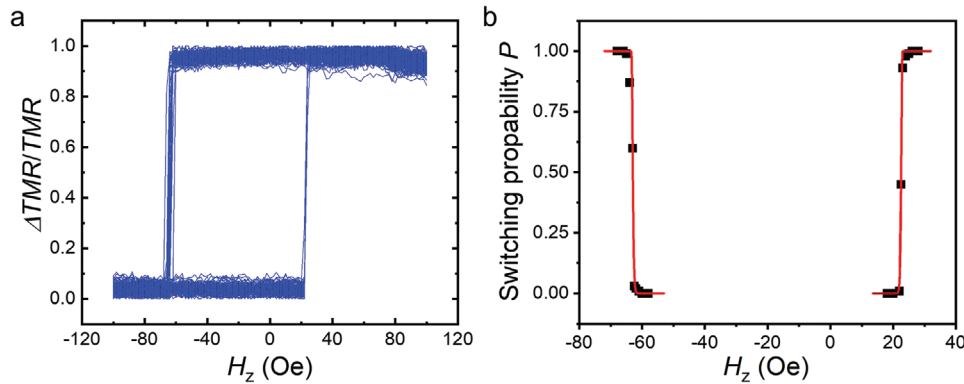
Figure 5. Thermal stability test in the nanoscale TI-pMTJ device. a) Minor normalized ΔTMR/TMR–H_z loops are measured for 100 times by using the nanoscale TI-pMTJ device with a MTJ diameter of 800 nm. b) Switching probability P as a function of H_z, where the red line represents the fitting curve by Equation (1).

Next, we evaluate the thermal stability factor Δ ($E_b/k_B T$) of the nanoscale TI-pMTJ devices by using the switching probability test based on the Stoner–Wohlfarth model:[46]

$$P(\tau) = 1 - \exp\left\{ -\frac{\tau}{\tau_0} \exp\left[-\Delta\left(1 - \frac{H - H_s}{H_k}\right)^2 \right] \right\} \quad (1)$$

where E_b is the energy barrier for switching, $k_B T$ is the thermal energy, P is the switching possibility, τ is the pulse duration time (1 s) of external magnetic field H (here is H_z), and τ_0 is the inverse of attempt frequency (1 ns). Although the Stoner–Wohlfarth model is based on a macrospin approximation, it can still give an accurate enough description on the time-scale associated with the magnetization switching and particularly it can provide a useful analytical understanding. As shown in Figure 4c, the analytical results (red curves) compare reasonably well with a full micromagnetic simulations (black curve) in predicting the critical SOT current density as a function of the STT current density. We have measured the minor normalized ΔTMR/TMR–H_z loops of the nanoscale TI-pMTJ device for 100 times to obtain the switching possibility P, as shown in **Figure 5**a, where only the CoFeB recording layer is switched back and forth. The shift of the loop center is mainly caused by the stray field originating from the incompletely compensated magnetization of the pinning layer.[47,48] Figure 5b shows the H_z dependence of P, by fitting the PH_z curve with Equation (1), the thermal stability factor $\Delta = 66$ is obtained for nanoscale TI-pMTJ, which meets the criteria ($\Delta = 60$) for the 10-years retention time of MRAM.[1]

To quantify the SOT efficiency, the film ii) (BiSb)$_2$Te$_3$/Ti/Co$_{20}$Fe$_{60}$B$_{20}$/MgO with the same structure as the recording layer in MTJs is prepared and patterned into Hall-bar devices. **Figure 6**a shows the anomalous Hall effect (AHE) loop of sample (ii), and the sharp-square loop indicates the strong PMA. Next, the SOT-induced magnetization switching is measured by sweeping the current pulse along the x direction, where the magnetization is detected by the Hall resistance R_{Hall}. Consequently, the nonvolatile magnetization switching can be achieved under $H_x = \pm100$ Oe as shown in Figure 6b. Figure 6c summarizes the H_x dependences of J_{cri} both in TI-pMTJ devices and TI-Hall-bar devices. Importantly, the J_{cri} in TI-pMTJ is very close to that in TI-Hall-bar devices, indicating the similar SOT properties in TI-pMTJ and TI-Hall-bar devices. Then, the harmonic Hall method is employed to quantify the SOT efficiency (charge–spin conversion efficiency) θ_{SH}: a sinusoidal ac current with a frequency of 13.33 Hz is applied along the x direction, with an in-plane magnetic field sweeping along the x direction. The SOT-induced effective field H_{SOT} exerts the oscillation of **M**, contributing to the 2ω Hall signal . When H_x is larger than the magnetic anisotropy field H_k, can be expressed as:[49,50]

$$R_{xy}^{2\omega} = \frac{R_A}{2}\frac{H_{DL}}{|H_x| - H_k} + R_p\frac{H_{FL}}{|H_x|} + R_{ANE+SSE}\frac{H_x}{|H_x|} + R_{offset} \quad (2)$$

where, R_A and R_P represent the anomalous Hall resistance and planar Hall resistance, respectively. $R_{ANE+SSE}$ is the thermal contribution from the anomalous Nernst and spin Seebeck effects, and R_{offset} is the offset signal. The first and second terms of Equation (2) originate from the SOT-induced damping-like (H_{DL}) and field-like (H_{FL}) contributions, respectively.

Figure 6d,e show the 1st and 2nd harmonic Hall resistance as a function of H_x in the TI-Hall-bar device with $J_e = 2.54 \times 10^4$ A cm^{-2}. The shows a non-linear dependence with H_x and reduces rapidly at the stronger magnetic field due to the suppression of the magnetic oscillation, indicating that the signals come from the SOT effect rather than the thermally induced ordinary Nernst effect.[51] By fitting the curve using Equation (2), the damp-like effective field H_{DL} can be obtained. Figure 6f shows the H_{DL} as a function of J_e. From the linear-fitting, the SOT-induced effective field $|\beta_{DL}|$ can be obtained of $|\beta_{DL}| = H_{DL}/J_e = 43.86 \times 10^{-6}$ Oe A^{-1} cm^2. Then, the SOT efficiency θ_{SH} is calculated by $|\theta_{SH}| = (2eM_s t_{FM}/\bar{h})\cdot|\beta_{DL}|$, where e is electron charge, M_s is the saturation magnetization, t_{FM} is the thickness of FM layer, and $\bar{h}$ is the reduced Planck constant. The $|\theta_{SH}|$ of (BiSb)$_2$Te$_3$ obtained by the second harmonic Hall method is $\approx$1.16 at room temperature, which is one order of magnitude larger than that in the HM-based system, supporting the ultralow switching current density of SOT.

Table 1 summarizes the crucial SOT performances of field-free SOT-MRAM devices, such as MTJ type, field-free method, $|\theta_{SH}|$ and J_{cri}. First, we can see that $|\theta_{SH}|$ in TI-MTJ is one order of magnitude large than that in HM-MTJ, consequently, J_{cri} in TI-MTJ is
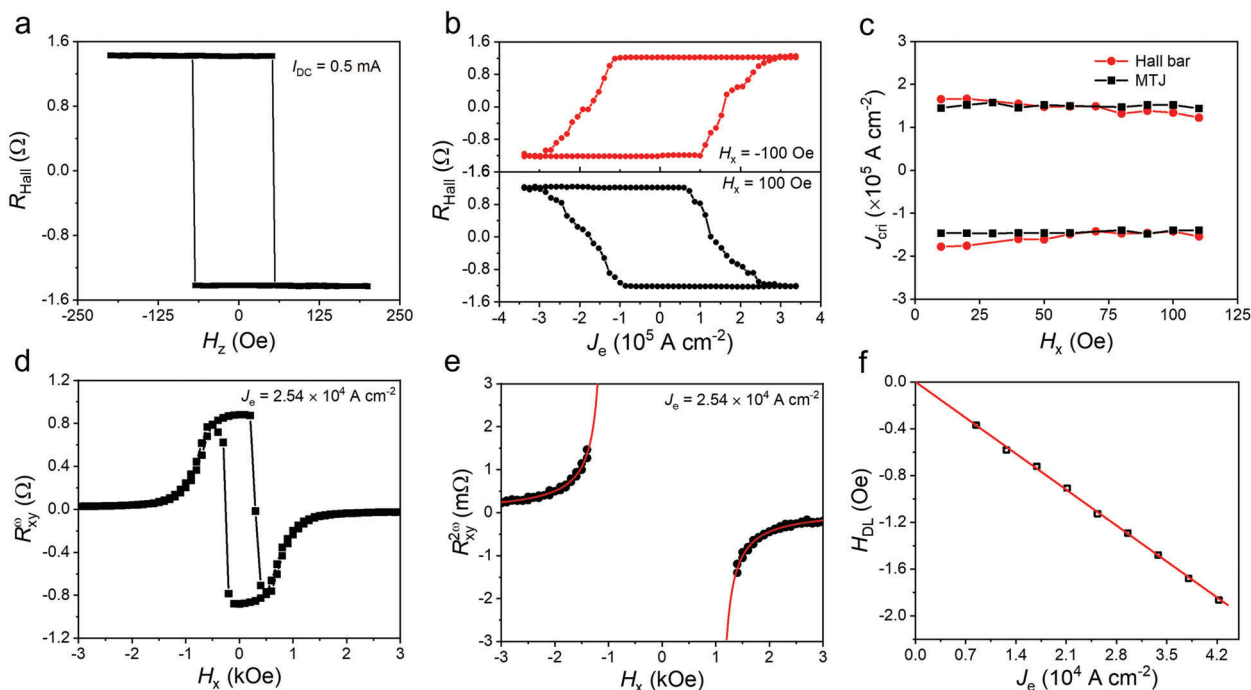
ADVANCED
SCIENCE NEWS

www.advancedsciencenews.com

ADVANCED
MATERIALS

www.advmat.de

Figure 6. Anomalous Hall effect (AHE) and harmonic Hall measurements of the Hall-bar devices with the structure of $(BiSb)_2Te_3(6)/Ti(5)/Co_{20}Fe_{60}B_{20}(1)/MgO(2)/Ta(2)$. a) AHE loop with an applied direct current $I_{DC} = 0.5$ mA. b) Current-driven SOT switching with $H_x = \pm100$ Oe, respectively. c) Critical switching current density (J_{cri}) as a function of H_x for the matters of TI-Hall-bar and TI-pMTJ devices. d,e) 1ω and 2ω harmonic Hall resistances (and) as functions of H_x, respectively. f) Current density dependence of damping-like effective field (H_{DL}), where the red-linear line is the fitting curve.

1–3 orders lower than that in HM-MTJ. Second, for the same SOT materials of $(BiSb)_2Te_3$, STT-assisted J_{cri} in perpendicular MTJ is still lower than that in the in-plane MTJ case (i.e., EA $//\sigma$) at the same time with an improved thermal stability. These suggest that perpendicular SOT-MRAM based on the STT-assisted field-free writing in TI-pMTJ devices has the advantages of low switching current density, high integration density, and high thermal stability.

3. Conclusions

We have experimentally demonstrated the functional 3-terminal perpendicular SOT-MRAM device with the topological insulator $(BiSb)_2Te_3$ writing channel, where the TMR of pMTJ is employed for the effective reading method. The ultralow switching current density of 1.5×10^5 A cm^{-2} is achieved in the TI-pMTJ device at room temperature, which is 1–2 orders of magnitude lower than that in conventional HM-based systems. With the assistance of a small STT current across the MTJ stack during SOT, the field-free deterministic SOT switching is realized, and the critical switching current density of SOT decreases with increasing the STT current density and is further reduced to the order of 10^4 A cm^{-2}. The large SOT efficiency (charge–spin conversion efficiency) θ_{SH} of 1.16 is obtained by the second harmonic Hall method, supporting the ultralow switching current density of SOT. At the same time, the nanoscale TI-pMTJ device shows a thermal stability factor of 66, showing the potential for over 10-years retention time.

Table 1. Crucial SOT performances of field-free SOT-MRAM devices based on different SOT materials and magnetic configurations, where $|\theta_{SH}|$ is the SOT efficiency, J_{cri} is the critical switching current density, MHM and EA respectively mean the magnetic hard mask and the easy axis, σ is the spin polarization.

SOT materials	MTJ type	Field-free method	$|\theta_{SH}|$	J_{cri} [10^5 A cm^{-2}]
Ta	perpendicular	STT-assisted	0.13	30–50[48]
Heavy metal bi-layer	perpendicular	STT-assisted	0.27	160[52]
Composite TaN/W	perpendicular	STT-assisted	0.27	25[53]
W	perpendicular	Co MHM	0.32	1260[14]
W	in-plane	canted SOT	0.37	236[15]
$(BiSb)_2Te_3$	in-plane	EA $// \sigma$	1.59	2–7[33]
$(BiSb)_2Te_3$	perpendicular	STT-assisted	1.16	0.93–1.17 (This work)

These results demonstrate the perpendicular SOT-MRAM driven by topological insulator writing channels with low-power, high-density, and high-endurance/retention, inspiring the revolution of SOT-MRAM from classical to quantum materials.

4. Experimental Section

Film Growth: The 6 nm-thick TI [$(Bi_{0.2}Sb_{0.8})_2Te_3$] films were grown by the co-evaporation (utilizing the high-purity Bi (99.9999%), Te (99.9999%) and Sb (99.999%) cells) on the Al_2O_3(0001) substrates via using an ultrahigh-vacuum MBE system. Before the evaporation, the Al_2O_3 substrate was pre-annealed at 700 °C to clean the surface in the vacuum chamber. During the TI growth, the substrate temperature was 200 °C and the Bi, Sb, Te cells were kept at 457 °C, 387 °C, and 340 °C, respectively. The in situ reflection high energy electron diffraction (RHEED) was used to monitor the layer-by-layer epitaxial growth of TI. Then, the p-MTJ stacks of Ti(5 nm)/$Co_{20}Fe_{60}B_{20}$(1 nm)/MgO(1.6 nm)/$Co_{20}Fe_{60}B_{20}$(1.1 nm)/-Ta(0.5 nm)/[Co(0.4 nm)/Pt(1.5 nm)]$_2$/Co(0.4 nm)/Ru(0.85 nm)/-[Co(0.4 nm)/Pt(1 nm)]$_3$/Ru(5 nm) and sandwich stacks of Ti(5 nm)/$Co_{20}Fe_{60}B_{20}$(1 nm)/MgO(2 nm)/Ta(2 nm) were deposited on TI by using a Singulus ROTARIS magnetron sputtering system at room temperature with a base pressure of 1×10^{-6} Pa.

Device Fabrication: The 3-terminal SOT-MRAM devices were fabricated by using two photolithography, one electron-beam lithography (EBL) and two Ar ion milling steps. To avoid the chemical degradation of the TI films during the device fabrication, a 300 nm layer of poly(methyl methacrylate) (PMMA, MircoChem, 495 PMMA A4) was first spin-coated on top of the film before the first photolithography step. We performed a photolithography process with an AZ2020 negative-tone resist to pattern the TI underlayer. After removing the PMMA layer by O_2 plasma, we etched all the layers using Ar ion milling, which was followed by the removal of the photoresist using acetone. Subsequently, MTJ pillars in circular shape with diameter ranging from 800 nm to 3 μm were patterned using electron beam lithography with a ma-N 2403 negative-tone resist. After etching the film up to Ti layer, a 30 nm-thick SiO_2 film was sputtered to electrically separate the top the bottom contacts of the tunnel junctions. Then, a second photolithography step with AZ5214 positive-tone photoresist was performed to pattern the electrodes, which was followed by sputtering Ti (10 nm) and Au (80 nm) layers. Finally, the fully patterned TI-MTJ devices were annealed in a vacuum at 250 °C for 0.5 h with a perpendicular magnetic field of 8 kOe.

Electrical and Magnetic Measurement: The SOT switching in the Hall bar and 3-terminal TI-pMTJ devices was measured by a probe station system with a magnet, where a two-channel Keithley 2612B source-meter was used to apply the current and measure the voltage. For the field-free switching measurements of 3-terminal TI-pMTJ devices, a Keithley 6221 current source was used to apply the STT current. For the harmonic Hall measurement, a Keithley 6221 current source was used to apply the ac current and two lock-in amplifiers (Stanford Research SR-830) were used to measure the harmonic Hall voltage. The magnetic properties of the TI-pMTJ stack were measured by a superconducting quantum interfere device (SQUID). All measurements were performed at room temperature.

Micromagnetic Simulation: The micromagnetic simulations were performed utilizing the GPU-accelerated software Mumax3 at the temperature of 300 K.[54] The magnetization dynamics was obtained by solving the Landau–Lifshit–Gilbert equation with additional SOT and STT terms, which can be described as:[48]

$$\frac{d\mathbf{m}}{dt} = -\gamma(\mathbf{m} \times \mathbf{H}) + \alpha\left(\mathbf{m} \times \frac{d\mathbf{m}}{dt}\right) + \frac{\gamma\hbar pJ_{STT}}{2t_{FM}eM_s}(\mathbf{m} \times \mathbf{m}_p \times \mathbf{m})$$

$$+ \frac{\gamma\xi_{STT}\hbar pJ_{STT}}{2t_{FM}eM_s}(\mathbf{m} \times \mathbf{m}_p) + \frac{\gamma\hbar\theta_{SH}J_{SOT}}{2t_{FM}eM_s}(\mathbf{m} \times \sigma \times \mathbf{m})$$

$$+ \frac{\gamma\xi_{SOT}\hbar\theta_{SH}J_{SOT}}{2t_{FM}eM_s}(\mathbf{m} \times \sigma) \tag{3}$$

where γ is the gyromagnetic ratio, α is the Gilbert damping constant, ξ_{STT} (ξ_{SOT}) is the ratio of field-like torque to damping-like torque of the STT(SOT), $\mathbf{m}_p$ and σ are the polarization directions of STT and SOT, $\hbar$ is the reduced Planck constant, t_{FM} is the thickness of the magnetic layer, e is the electron charge, M_s is the saturation magnetization, p is the spin polarization constant, θ_{SH} is the SOT efficiency, and J_{STT} (J_{SOT}) is the charge current density of STT(SOT). In our simulations, $\alpha = 0.015$,[55,56] $\xi_{STT} = 0$, $\xi_{SOT} = 0.14$, $\mathbf{m}_p = (0, 0, 1)$, $\sigma = (0, 1, 0)$, $p = 0.4$, and $\theta_{SH} = 1.16$. In the MTJ, the radius of the free layer r was 400 nm and the thickness w was 1 nm. The mesh was $2 \times 2 \times 1$ nm^3. In addition, the Heisenberg exchange constant A was set to 10 pJ m^{-1},[57–59] the saturation magnetization M_s was equal to 868 kA m^{-1} measured by the SQUID. Due to the effective anisotropy field H_{keff} of 0.2 T, the perpendicular magnetic anisotropy K_u was equal to 0.56 MJ m^{-3}.

Supporting Information

Supporting Information is available from the Wiley Online Library or from the author.

Conflict of Interest

The authors declare no conflict of interest.

Data Availability Statement

The data that support the findings of this study are available from the corresponding author upon reasonable request.

[1] S. Bhatti, R. Sbiaa, A. Hirohata, H. Ohno, S. Fukami, S. N. Piramanayagam, *Mater. Today* **2017**, *20*, 530.
[2] T. Miyazaki, N. Tezuka, *J. Magn. Magn. Mater.* **1995**, *139*, L231.
[3] J. S. Moodera, L. R. Kinder, T. M. Wong, R. Meservey, *Phys. Rev. Lett.* **1995**, *74*, 3273.

**ADVANCED
SCIENCE NEWS**

www.advancedsciencenews.com

**ADVANCED
MATERIALS**

www.advmat.de

[4] W. H. Butler, X.-G. Zhang, T. C. Schulthess, J. M. MacLaren, *Phys. Rev. B* **2001**, *63*, 054416.

[5] S. S. P. Parkin, C. Kaiser, A. Panchula, P. M. Rice, B. Hughes, M. Samant, S.-H. Yang, *Nat. Mater.* **2004**, *3*, 862.

[6] S. Yuasa, T. Nagahama, A. Fukushima, Y. Suzuki, K. Ando, *Nat. Mater.* **2004**, *3*, 868.

[7] K. C. Chun, H. Zhao, J. D. Harms, T.-H. Kim, J.-P. Wang, C. H. Kim, *IEEE J. Solid-State Circuits* **2013**, *48*, 598.

[8] W. S. Zhao, Y. Zhang, T. Devolder, J. O. Klein, D. Ravelosona, C. Chappert, P. Mazoyer, *Microelectron. Reliab.* **2012**, *52*, 1848.

[9] S. Z. Rahaman, I.-J. Wang, D.-Y. Wang, C.-F. Pai, Y.-C. Hsin, S.-Y. Yang, H.-H. Lee, Y.-J. Chang, Y.-C. Kuo, Y.-H. Su, G.-L. Chen, F.-M. Chen, J.-H. Wei, T.-H. Hou, S.-S. Sheu, C.-I. Wu, D.-L. Deng, *IEEE J. Electron Devices Soc.* **2020**, *8*, 163.

[10] N. Sato, F. Xue, R. M. White, C. Bi, S. X. Wang, *Nat. Electron.* **2018**, *1*, 508.

[11] M. Wang, W. Cai, D. Zhu, Z. Wang, J. Kan, Z. Zhao, K. Cao, Z. Wang, Y. Zhang, T. Zhang, C. Park, J.-P. Wang, A. Fert, W. Zhao, *Nat. Electron.* **2018**, *1*, 582.

[12] K. Garello, F. Yasin, S. Couet, L. Souriau, J. Swerts, S. Rao, S. Van Beek, W. Kim, E. Liu, S. Kundu, D. Tsvetanova, K. Croes, N. Jossart, E. Grimaldi, M. Baumgartner, D. Crotti, A. Fumemont, P. Gambardella, G. S. Kar, in *2018 IEEE Symp. on VLSI Circuits*, IEEE, Piscataway, NJ, USA, **2018**, pp. 81–82.

[13] W. J. Kong, C. H. Wan, C. Y. Guo, C. Fang, B. S. Tao, X. Wang, X. F. Han, *Appl. Phys. Lett.* **2020**, *116*, 162401.

[14] K. Garello, F. Yasin, H. Hody, S. Couet, L. Souriau, S. H. Sharifi, J. Swerts, R. Carpenter, S. Rao, W. Kim, J. Wu, K. K. V. Sethu, M. Pak, N. Jossart, D. Crotti, A. Furnemont, G. S. Kar, in *2019 Symp. on VLSI Circuits*, IEEE, Piscataway, NJ, USA, **2019**, pp. T194–T195.

[15] H. Honjo, T. V. A. Nguyen, T. Watanabe. T. Nasuno, C. Zhang, T. Tanigawa, S. Miura, H. Inoue, M. Niwa, T. Yoshiduka, Y. Noguchi, M. Yasuhira, A. Tamakoshi, M. Natsui, Y. Ma, H. Koike, Y. Takahashi, K. Furuya, H. Shen, S. Fukami, H. Sato, S. Ikeda, T. Hanyu, T. Ohno, T. Endoh, in *2019 IEEE Int. Electron Devices Meeting (IEDM)*, IEEE, Piscataway, NJ, USA, **2019**, https://doi.org/10.1109/IEDM19573.2019.8993443.

[16] D. Go, H.-W. Lee, *Phys. Rev. Res.* **2020**, *2*, 013177.

[17] S. Ding, A. Ross, D. Go, L. Baldrati, Z. Ren, F. Freimuth, S. Becker, F. Kammerbauer, J. Yang, G. Jakob, Y. Mokrousov, M. Kläui, *Phys. Rev. Lett.* **2020**, *125*, 177201.

[18] L. Liao, F. Xue, L. Han, J. Kim, R. Zhang, L. Li, J. Liu, X. Kou, C. Song, F. Pan, Y. Otani, *Phys. Rev. B* **2022**, *105*, 104434.

[19] M. I. Dyakonov, V. I. Perel, *Phys. Lett. A* **1971**, *35*, 459.

[20] J. E. Hirsch, *Phys. Rev. Lett.* **1999**, *83*, 1834.

[21] Y. A. Bychkov, E. I. Rashba, *J. Exp. Theor. Phys. Lett.* **1984**, *39*, 78.

[22] I. M. Miron, K. Garello, G. Gaudin, P.-J. Zermatten, M. V. Costache, S. Auffret, S. Bandiera, B. Rodmacq, A. Schuhl, P. Gambardella, *Nature* **2011**, *476*, 189.

[23] L. Liu, O. J. Lee, T. J. Gudmundsen, D. C. Ralph, R. A. Buhrman, *Phys. Rev. Lett.* **2012**, *109*, 096602.

[24] L. Liu, C.-F. Pai, D. C. Ralph, R. A. Buhrman, *Phys. Rev. Lett.* **2012**, *109*, 186602.

[25] L. Liu, C.-F. Pai, Y. Li, H. W. Tseng, D. C. Ralph, R. A. Buhrman, *Science* **2012**, *336*, 555.

[26] G. Yu, P. Upadhyaya, Y. Fan, J. G. Alzate, W. Jiang, K. L. Wong, S. Takei, S. A. Bender, L.-T Chang, Y. Jiang, M. Lang, J. Tang, Y. Wang, Y. Tserkovnyak, P. K. Amiri, Kang L. Wang, *Nat. Nanotechnol.* **2014**, *9*, 548.

[27] J. Ryu, S. Lee, K.-J. Lee, B.-G. Park, *Adv. Mater.* **2020**, *32*, 1907148.

[28] Y. Fan, X. Kou, P. Upadhyaya, Q. Shao, L. Pan, M. Lang, X. Che, J. Tang, M. Montazeri, K. Murata, L.-T. Chang, M. Akyol, G. Yu, T. Nie, K. L. Wong, J. Liu, Y. Wang, Y. Tserkovnyak, K. L. Wang, *Nat. Nanotech.* **2016**, *11*, 352.

[29] Y. Wang, P. Deorani, K. Banerjee, N. Koirala, M. Brahlek, S. Oh, H. Yang, *Phys. Rev. Lett.* **2015**, *114*, 257202.

[30] K. Yasuda, A. Tsukazaki, R. Yoshimi, K. Kondou, K. S. Takahashi, Y. Otani, M. Kawasaki, Y. Tokura, *Phys. Rev. Lett.* **2017**, *119*, 137-204.

[31] X. Che, Q. Pan, B. Vareskic, J. Zou, L. Pan, P. Zhang, G. Yin, H. Wu, Q. Shao, P. Deng, K. L. Wang, *Adv. Mater.* **2020**, *32*, 1907661.

[32] J. Han, A. Richardella, S. A. Siddiqui, J. Finley, N. Samarth, L. Liu, *Phys. Rev. Lett.* **2017**, *119*, 077702.

[33] H. Wu, A. Chen, P. Zhang, H. He, J. Nance, C. Guo, J. Sasaki, T. Shirokura, P. N. Hai, B. Fang, S. A. Razavi, K. Wong, Y. Wen, Y. Ma, G. Yu, G. P. Carman, X. Han, X. Zhang, K. L. Wang, *Nat. Commun.* **2021**, *12*, 6251.

[34] H. Wu, Y. Xu, P. Deng, Q. Pan, S. A. Razavi, K. Wong, L. Huang, B. Dai, Q. Shao, G. Yu, X. Han, J. Rojas-Sánchez, S. Mangin, K. L. Wang, *Adv. Mater.* **2019**, *31*, 1901681.

[35] P. Li, W. Wu, Y. Wen, C. Zhang, J. Zhang, S. Zhang, Z. Yu, S. A. Yang, A. Manchon, X. Zhang, *Nat. Commun.* **2018**, *9*, 3990.

[36] Y. Wang, D. Zhu, Y. Wu, Y. Yang, J. Yu, R. Ramaswamy, R. Mishra, S. Shi, M. Elyasi, K.-L. Teo, Y. Wu, H. Yang, *Nat. Commun.* **2017**, *8*, 1364.

[37] M. Dc, R. Grassi, J.-Y. Chen, M. Jamali, D. Reifsnyder Hickey, D. Zhang, Z. Zhao, H. Li, P. Quarterman, Y. Lv, M. Li, A. Manchon, K. A. Mkhoyan, T. Low, J.-P. Wang, *Nat. Mater.* **2018**, *17*, 800.

[38] H. Wu, P. Zhang, P. Deng, Q. Lan, Q. Pan, S. A. Razavi, X. Che, L. Huang, B. Dai, K. Wong, X. Han, K. L. Wang, *Phys. Rev. Lett.* **2019**, *123*, 207205.

[39] N. H. D. Khang, Y. Ueda, P. N. Hai, *Nat. Mater.* **2018**, *17*, 808.

[40] T.-Y. Chen, C.-W. Peng, T.-Y. Tsai, W.-B. Liao, C.-T. Wu, H.-W. Yen, C.-F. Pai, *ACS Appl. Mater. Interfaces* **2020**, *12*, 7788.

[41] P. Deorani, J. Son, K. Banerjee, N. Koirala, M. Brahlek, S. Oh, H. Yang, *Phys. Rev. B* **2014**, *90*, 094403.

[42] V. Sharma, W. Wu, P. Bajracharya, D. Q. To, A. Johnson, A. Janotti, G. W. Bryant, L. Gundlach, M. B. Jungfleisch, R. C. Budhani, *Phys Rev.* **2021**, *5*, 124410.

[43] C. Du, H. Wang, F. Yang, P. C. Hammel, *Phys. Rev. B* **2014**, *90*, 140407.

[44] C.-Z. Chang, J. Zhang, X. Feng, J. Shen, Z. Zhang, M. Guo, K. Li, Y. Ou, P. Wei, L.-L. Wang, Z.-Q. Ji, Y. Feng, S. Ji, X. Chen, J. Jia, X. Dai, Z. Fang, S.-C. Zhang, K. He, Y. Wang, L. Lu, X.-C. Ma, Q.-K. Xue, *Science* **2013**, *340*, 167.

[45] X. Kou, S.-T. Guo, Y. Fan, L. Pan, M. Lang, Y. Jiang, Q. Shao, T. Nie, K. Murata, J. Tang, Y. Wang, L. He, T.-K. Lee, W.-L. Lee, K. L. Wang, *Phys. Rev. Lett.* **2014**, *113*, 137201.

[46] H. Sato, M. Yamanouchi, K. Miura, S. Ikeda, R. Koizumi, F. Matsukura, H. Ohno, *IEEE Magn. Lett.* **2012**, *3*, 3000204.

[47] Me. Wang, W. Cai, D. Zhu, Z. Wang, J. Kan, Z. Zhao, K. Cao, Z. Wang, Y. Zhang, T. Zhang, C. Park, J-P Wang, A. Fert, W. Zhao, *Nat. Electron.* **2018**, *1*, 582.

[48] M. Wang, W. Cai, K. Cao, J. Zhou, J. Wrona, S. Peng, H. Yang, J. Wei, W. Kang, Y. Zhang, J. Langer, B. Ocker, A. Fert, W. Zhao, *Nat. Commun.* **2018**, *9*, 671.

[49] M. Hayashi, J. Kim, M. Yamanouchi, H. Ohno, *Phys. Rev. B* **2014**, *89*, 144425.

[50] C. O. Avci, K. Garello, M. Gabureac, A. Ghosh, A. Fuhrer, S. F. Alvarado, P. Gambardella, *Phys. Rev. B* **2014**, *90*, 224427.

[51] N. Roschewsky, E. S. Walker, P. Gowtham, S. Muschinske, F. Hellman, S. R. Bank, S. Salahuddin, *Phys. Rev. B* **2019**, *99*, 195103.

[52] N. Sato, G. A. Allen, W. P. Benson, B. Buford, A. Chakraborty, M. Christenson, T. A. Gosavi, P. E. Heil, N. A. Kabir, B. J. Krist, K. P. O'Brien, K. Oguz, R. R. Patil, J. Pellegren, A. K. Smith, E. S. Walker, P. J. Hentges, M. V. Metz, M. Seth, B. Turkot, C. J. Wiegand, H. J. Yoo, I. A. Young, in *2020 IEEE Symp. on VLSI Technology*, IEEE, Piscataway, NJ, USA, **2020**, https://doi.org/10.1109/VLSITechnology18217.2020.9265028.

[53] Y.-J. Tsou, K.-S. Li, J.-M. Shieh, W.-J. Chen, H.-C. Chen, Y.-J. Chen, C.-L. Hsu, Y.-M. Huang, F.-K. Hsueh, W.-H. Huang, W.-K. Yeh, H.-C. Shih, P.-C. Liu, C. W. Liu, Y.-S. Yen, C.-H. Lai, J.-H. Wei, D. D. Tang, J. Y.-C. Sun, in *2021 Symp. on VLSI Technology*, IEEE, Piscataway, NJ, USA, **2021**, pp. 1–2.

[54] A. Vansteenkiste, J. Leliaert, M. Dvornik, M. Helsen, F. Garcia-Sanchez, B. Van Waeyenberge, *AIP Adv.* **2014**, *4*, 107133.

[55] C. Burrowes, N. Vernier, J.-P. Adam, L. Herrera Diez, K. Garcia, I. Barisic, G. Agnus, S. Eimer, J.-V. Kim, T. Devolder, A. Lamperti, R. Mantovan, B. Ockert, E. E. Fullerton, D. Ravelosona, *Appl. Phys. Lett.* **2013**, *103*, 182401.

[56] L. H. Diez, M. Voto, A. Casiraghi, M. Belmeguenai, Y. Roussigné, G. Durin, A. Lamperti, R. Mantovan, V. Sluka, V. Jeudy, Y. T. Liu, A. Stashkevich, S. M. Chérif, J. Langer, B. Ocker, L. Lopez-Diaz, D. Ravelosona, *Phys. Rev. B* **2019**, *99*, 054431.

[57] M. Yamanouchi, A. Jander, P. Dhagat, S. Ikeda, F. Matsukura, H. Ohno, *IEEE Magn. Lett.* **2011**, *2*, 3000304.

[58] M. Cubukcu, J. Sampaio, K. Bouzehouane, D. Apalkov, A. V. Khvalkovskiy, V. Cros, N. Reyren, *Phys. Rev. B* **2016**, *93*, 020401.

[59] S. Jaiswal, K. Litzius, I. Lemesh, F. Büttner, S. Finizio, J. Raabe, M. Weigand, K. Lee, J. Langer, B. Ocker, G. Jakob, G. S. D. Beach, M. Kläui, *Appl. Phys. Lett.* **2017**, *111*, 022409.